IS-PORTO 2023 PROCEEDINGS

Proceedings of the 8th International Symposium on DEFORMATION CHARACTERISTICS OF GEOMATERIALS Porto, 3rd - 6th September 2023

High-precision and high-accuracy stereophotogrammetric image analysis for small to large strain deformation measurement in triaxial apparatus

Satoshi Nishimura[1#]

[1]*Hokkaido University, Faculty of Engineering, Kita-8 Nishi-13, Kita-Ku, Sapporo, Japan*
[#]*Corresponding author: nishimura@eng.hokudai.ac.jp*

ABSTRACT

A deformation measurement system for laboratory soil testing based on stereophotogrammetric image analysis was developed with a purpose of characterising soil behaviour continuously from small to large strains. The system is applicable to triaxial tests with pressure chamber and confining fluid by correcting the refraction-induced distortion of images by ray tracing. In comparison to similar existing studies, the present study put priority in precision and accuracy in relative displacement tracking, which is the key feature in resolving small strain in soil specimen and characterising its stiffness. The displacement tracking is performed with a hybrid algorithm combining Particle Tracking Velocimetry (PTV) for primary target matching and subpixel Digital Image Correlation (DIC) for more precise image matching. The deformation of clay samples with and without end lubrication was compared by visualising the deformation at different levels of strain. This paper is basically a summary of Nishimura (2022). Another example of application in laboratory testing involving fine particle suffusion is also shown. Some notes on implementation of the technique for good practice and on future development are additionally described.

Keywords: deformation; stiffness; triaxial testing; image analysis.

1. Introduction

Measuring soil deformation in laboratory soil tests accurately over wide strain ranges has been one of the most eagerly pursued goals in this series of symposia. The keynote lecture on tomography analysis by Viggiani and Hall (2008) in Atlanta heralded a new stream of studies that exploited recent development of full-field imaging techniques for characterising soil deformation. Strain measurement based on optical imaging using digital cameras has also found a way into laboratory soil testing; for example, use of CCD units in a triaxial cell was presented by Tani et al. (2003) in IS-Lyon. Qiao et al. (2008) presented image analysis based on stereophotogrammetry to triaxial testing in IS-Atlanta. Later, Bhandari et al. (2011) introduced ray tracing technique to overcome the image distortion caused by ray refraction due to the triaxial cell wall and cell water when images are taken from outside the cell. Zhang et al. (2014) adopted this approach and developed a stereophotogrammetric method to capture three-dimensional displacement of the soil specimen surface from outside the triaxial cell. In the meantime, Nishimura et al. (2016) attempted to measure strains of 10^{-3}% with a standard compact digital camera in simpler, oedometric conditions by adopting subpixel Particle Image Velocimetry (PIV). These developments suggest a possibility that fully three-dimensional deformation of a soil sample in a triaxial cell can be captured to a resolution of 10^{-3}% strain only with a pair of ordinary digital cameras, when all the above techniques are combined and optimised. This study aimed at establishing such a new image-based strain measurement technique for laboratory soil testing, and exploring the best accuracy and precision that can be achieved with commonly available equipment. A comprehensive description of the proposed technique and the experimental exercise is given by Nishimura (2022). This paper provides a short summary of the principle and selected results, as well as reporting an extra example of application. For detailed formulation, refer to the above paper. A perspective of further development, in particular to overcome problems associated with highly deformable soils such as peats, will also be discussed as an update to the above published work.

2. Stereophotogrammetry with PTV-DIC hybrid approach

2.1. Principle of stereophotogrammetry

Stereophotogrammetry is a long-established method to reconstruct three-dimensional coordinates of an object that is observed by a pair of cameras based on epipolar geometry. The method typically assumes a pinhole camera model, in which the optical rays pass through a focal point and form an image on the cameras' image sensor. In triaxial tests, however, the rays coming from the sample surface undergo refraction twice before reaching the cameras; once at the cell water-wall

(typically made of acrylic resin) interface, and once at the wall-air interface, as shown in Fig. 1. Bhandari et al. (2011) and Zhang et al. (2014) presented how this effect is corrected for by the ray tracing technique. This study adopts the same approach in correcting for the refraction effect. The ray traced back from each camera, originating from a target image on the camera plane u-v, passing through the focal point, should meet at a single point, where the target physically exists. Mathematically, obtaining this target location is an indeterminate problem, and the coordinates are estimated by the least square optimisation. Zhang et al. (2014) proposed an approach of using a single camera but taking photographs from many different angles, and increasing the number of rays for more accurate absolute positioning of the target. In this study, however, two fixed cameras were used to take advantage of time-lapse, automatic shooting of images. Stationary cameras are also advantageous in achieving higher precision in relative positioning, when small-strain deformation is tracked. The ray vector $\mathbf{i_0}$ originating from the camera is expressed as:

$$i_0 = \left[i_{0,X_w}\ i_{0,Y_w}\ i_{0,Z_w}\right] = -R^{-1}t + \eta\left[\frac{\delta_u}{f}(u - u_0)\ \frac{\delta_v}{f}(v - v_0)\ 1\right] \quad (1)$$

Where $\mathbf{i_0}$ is expressed in the X_w-Y_w-Z_w coordinate system (hence the subscripts in the second equation). The factor η is an arbitrary scalar, and **R** and **t** are the rotation matrix and translation vector, respectively, between X_w-Y_w-Z_w and X-Y-Z coordinate systems. δ_u and δ_v are the pixel size in u and v directions, and (u_0, v_0) are the image centre in the camera's image plane u-v. f is the focal distance. The ray vector $\mathbf{i_0}$ is converted to the ray vector after refraction twice, $\mathbf{i_2}$, by applying Snell's law twice with the absolute refraction indices for the air n_a, acrylic resin n_c and water n_w (1.00, 1.49 and 1.33, respectively). Performing the least square optimisation as mentioned above means obtaining the best estimate of the target coordinates (X_w, Y_w, Z_w) representing the intersection point of the rays from right and left cameras from the following equation:

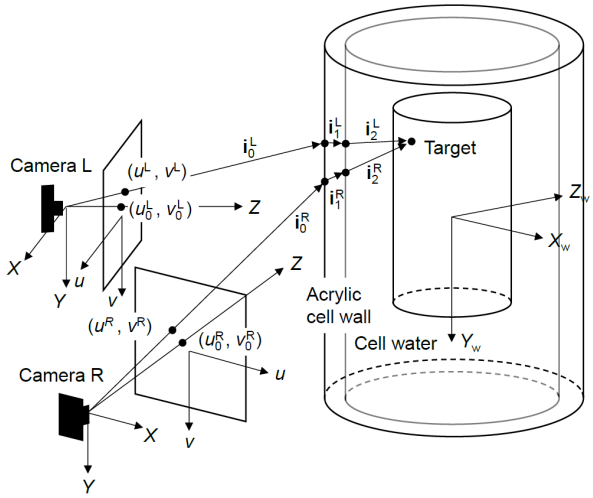

Figure 1. Geometry of stereophotogrammetry with ray refraction, applied to triaxial testing.

$$\begin{bmatrix} i^L_{2,Y_w} & -i^L_{2,X_w} & 0 \\ 0 & i^L_{2,Z_w} & -i^L_{2,Y_w} \\ -i^L_{2,Z_w} & 0 & i^L_{2,X_w} \\ i^R_{2,Y_w} & -i^R_{2,X_w} & 0 \\ 0 & i^R_{2,Z_w} & -i^R_{2,Y_w} \\ -i^R_{2,Z_w} & 0 & i^R_{2,X_w} \end{bmatrix} \begin{bmatrix} X_w \\ Y_w \\ Z_w \end{bmatrix} = \begin{bmatrix} i^L_{2,Y_w}X^L_{w2} - i^L_{2,X_w}Y^L_{w2} \\ i^L_{2,Z_w}Y^L_{w2} - i^L_{2,Y_w}Z^L_{w2} \\ i^L_{2,X_w}Z^L_{w2} - i^L_{2,Z_w}X^L_{w2} \\ i^R_{2,Y_w}X^R_{w2} - i^R_{2,X_w}Y^R_{w2} \\ i^R_{2,Z_w}Y^R_{w2} - i^R_{2,Y_w}Z^R_{w2} \\ i^R_{2,X_w}Z^R_{w2} - i^R_{2,Z_w}X^R_{w2} \end{bmatrix} \quad (2)$$

where $\mathbf{i_2} = (i_{2,X_w}, i_{2,Y_w}, i_{2,Z_w})$, and (X_{w2}, Y_{w2}, Z_{w2}) is the origin of $\mathbf{i_2}$ (i.e. the intersection of $\mathbf{i_2}$ and the cell's inner surface). Superscripts R and L represent the right and left cameras (and the rays from them), respectively.

2.2. Camera calibration

Tracing back the ray from the camera requires the camera's location and orientation in the real world coordinate system X_w-Y_w-Z_w, which is set for the cell centre as shown in Fig. 1. This 'extrinsic' information, as well as 'intrinsic' information (innate to cameras themselves) such as δ_u, δ_v, u_0, v_0 and f are obtained by calibration. In the proposed method, a sheet with regularly set target points is temporarily set on the cell wall surface, as shown in Fig. 2 (right), once the cameras are fixed in place and the zoom and focus were set on the specimen (Fig. 2, left). By taking images of the sheet surrounding the cell wall, the camera parameters are calibrated based on the known target coordinates (they are known from the cell wall's outer diameter). This method allows recalibration whenever cameras are moved, or their conditions (such as zoom) are changed. The conventional camera calibration method can be used, because the sheet is outside the cell and the images are refraction-free. The perspective projection matrix **P**, connecting the two coordinate systems X_w-Y_w-Z_w and u-v in the following equation is estimated from the known X_w, Y_w, Z_w, u and v values of all the targets; see Nishimura (2022) for more details.

$$[u\ v\ 1] = [A\ 0][R\ t\ 0\ 1][X_w\ Y_w\ Z_w\ 1] = P[X_w\ Y_w\ Z_w\ 1] \quad (3)$$

Matrix **A** mainly consists of the intrinsic parameters, and is obtained along with **R** and **t** by performing RQ-decomposition of **P**.

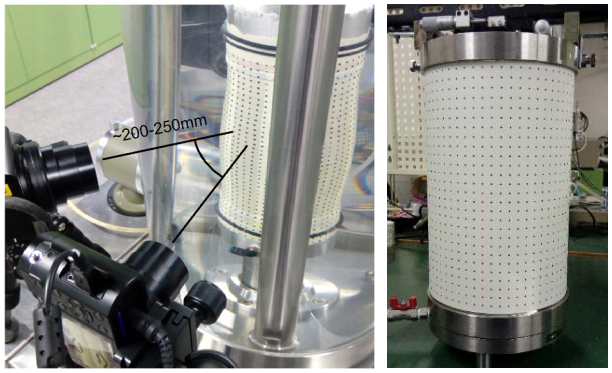

Figure 2. Two cameras set for soil specimen (left) and calibration sheet with target point surrounding the cell (right).

2.3. Target tracking: PTV-DIC hybrid approach

Once the location and the orientation of the cameras are established, the main input into the stereophotogrammetric analysis is the u-v coordinates of each target in each camera. How accurately and precisely the targets are tracked in each camera determines the accuracy and precision in reconstruction of the X_w-Y_w-Z_w coordinates of the targets in the real world. This study adopts a hybrid approach combining Particle Tracking Velocimetry (PTV) and subpixel Digital Image Correlation (DIC). The process is illustrated in Fig. 3. The images of the specimen are firstly transformed into binary (i.e. black and white), and the targets are obtained as 'blobs', or aggregates of black pixels. Each blob's centroid is measured as the target coordinates in the u-v plane. In computer vision, this processing is relatively fast. Although thus determined coordinates (this process is described as PTV in this paper; PTV has different algorithms in identifying particles) already have sub-pixel precision, relative displacement of a target between a pair of images can be refined by sub-pixel DIC in greyscale. The search range in DIC can be narrowed down to +/-1 pix by using the results of PTV as guide. This drastically reduces the computational effort involved in DIC. In this manner, the advantages of the fast operation in binary images and the precise inter-image displacement tracking in greyscale are exploited at the same time.

2.4. Target tracking in highly deformable soils

The above method works very well for many types of soils, including clays and sands, in the author's experience. For highly deformable soils, however, problems are anticipated in tracking the targets drawn on the rubber membrane. Fig. 4 shows the isotropic compression of peat up to 100 kPa. Although the targets are initially clear, the very large deformation (the volumetric strain reaching 50% in this case) engulfs some of the targets into the membrane wrinkles formed during the process. The procedures based on Fig. 3 will require modification, as some targets are no longer recognisable from the images. However, the displacement is still traceable with PIV only, as long as the deformation is slow relative to the photo shooting interval, and the targets are known to be somewhere very close to where they were in the previous reference image. In this case, the PTV part can be skipped automatically.

2.5. Accuracy, precision and suggestions for good practice

Fig. 5 shows a summary of the overall procedures of the displacement measurement of the targets on the specimen surfaces. This is a standard flow, but all the processes except for photo-shooting may be in fact performed after the test, including the camera calibration. The computing processes were encoded in Python using OpenCV 4.0 library. The typical computing time taken for each pair of images is about a second when run on a Core i7 PC.

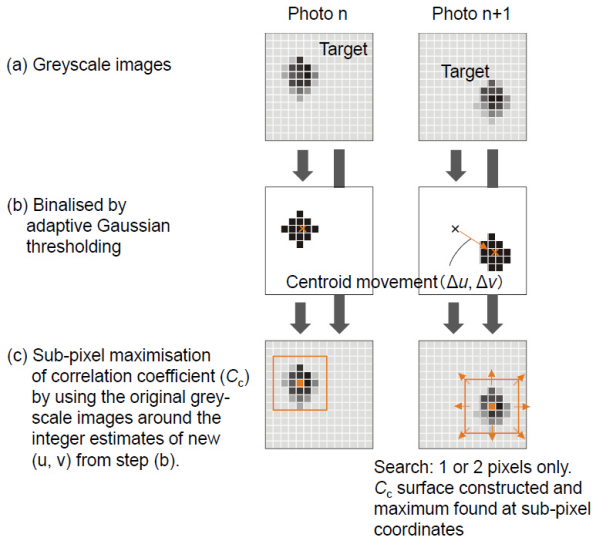

Figure 3. Process of PTV (binary) – DIC (greyscale) hybrid tracking of target particle.

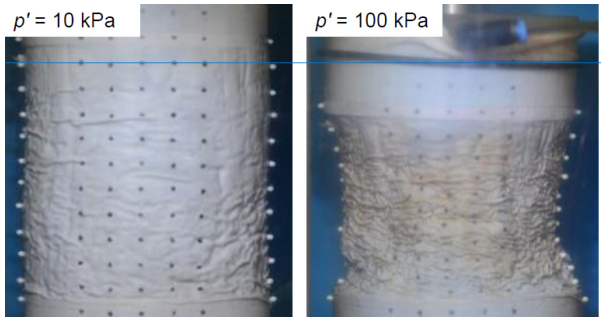

Figure 4. Difficulty of target recognition at large deformation.

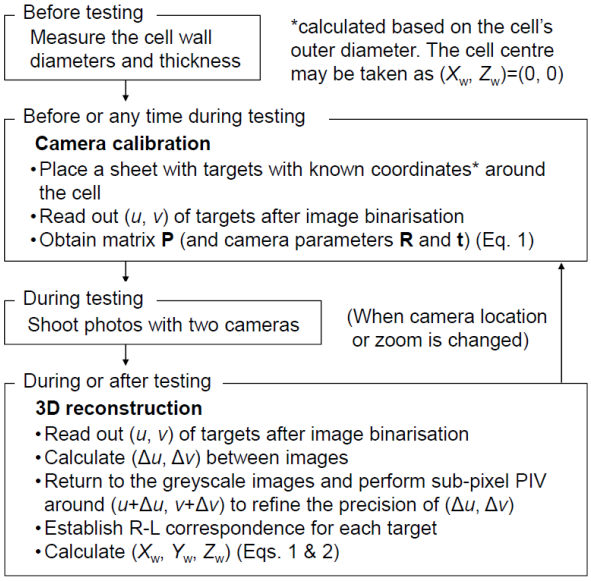

Figure 5. Whole process of image analysis during triaxial test.

The accuracy, or the closeness of measured displacement to a true value, was evaluated by moving a dummy specimen on a two- or three-DOF micrometer-controlled stages (allowing displacements in X_w-Z_w or X_w-Y_w-Z_w). The accuracy of the image analysis was approximately 1% over a span of 5 mm in every direction. The precision, or the consistency of multiple measurements, was evaluated for a stationary object. For a relative displacement (i.e. subtracting artefactual rigid-

body movement), a precision of 0.001 mm to 0.002 mm was achieved when moving average of five images was adopted, assuming that the deformation in real tests is sufficiently slow and allows many images to be taken.

With the code to perform the analysis, the proposed image analysis does not require special skills in principle. However, there are some points to be noted in achieving good accuracy and precision.

- Solid tripods are desirable, to prevent creeping camera movement during the photo shooting.
- Mock shutter sound, if any, should be cancelled, as it leads to faint vibration.
- Focus should be set manually, to prevent automatic focus each time an image is taken.
- A slower shutter speed should be adopted. This helps reduce noises and improve the precision.
- Using a structured pattern for the target points on the specimen surface (i.e. on the rubber membrane) simplifies the procedures, because the targets are easily labelled by column and row numbers, removing a need for stereo-matching based on image patterns.

3. Example of application: Triaxial compression tests on clay

3.1. Experimental conditions

Consolidated undrained triaxial tests on reconstituted saturated Kasaoka clay (the liquid limit w_L = 60% and the plastic limit w_P = 26%) were performed to demonstrate the strain measurement capability of the proposed image analysis. The nominal size of the specimens was 150 mm in height and 75 mm in diameter. After being preconsolidated one-dimensionally to 200 kPa in a consolidometer, the specimens were set into a triaxial cell, and subjected to three small-strain undrained axial loading and unloading cycles with an axial strain ε_a amplitude of 0.05% at $\dot{\varepsilon}_a$= 0.2%/hour, at the isotropic effective stress p' = 70 kPa. The specimen was then isotropically consolidated to 300 kPa and then allowed to swell to 250 kPa. It was subjected to the same cyclic loadings as above again, and then to monotonic undrained loading to ε_a = 0.15% at $\dot{\varepsilon}_a$ = 0.6%/hour. The results of one test with end lubrication and another without, as shown in Fig. 6, are discussed below.

Two pairs of cameras were used to observe the front and rear faces of the specimen, while sometimes they were relocated to observe the right and left faces. The deployed cameras were Panasonic Lumix TX1 with 3,648 pix by 4,864 pix, with a built-in time-lapse photo shooting function. The image sensor was a 1.0-inch MOS. They were commonly available middle-grade compact cameras.

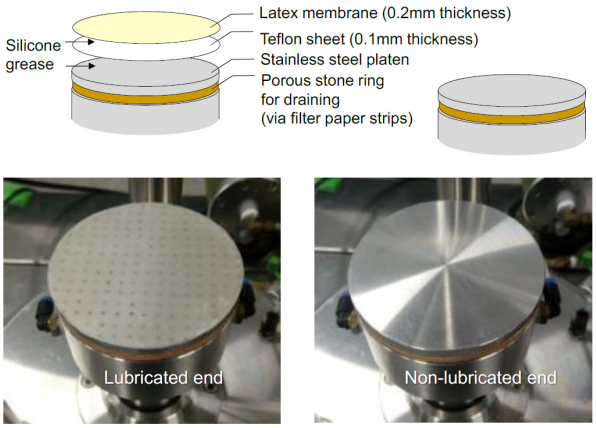

Figure 6. Lubricated and non-lubricated (polished steel) ends.

3.2. Small-strain behaviour

The deformation during the cyclic small-strain loadings was quantified in two manners; calculating strain (and then Young's modulus E and Poisson's ratio ν) as an average over the entire specimen height H, or over only the middle third $H/3$. The secant undrained Young's modulus $E_{u,sec}$ and Poisson's ratio ν measured are summarised in Table 1, in comparison with the global measurements. The latter are based on the loading ram movement measured outside the cell and the drained water volume from the specimen (deemed zero during undrained loading). The radial strain was calculated by assuming that the cylindrical shape of the specimen was maintained all the time. Under undrained conditions, this automatically leads to ν = 0.5 for small strains. The results show that the image analysis provides greater stiffness, by being free from the apparatus compliances and bedding errors, which are known to lead to underestimation of the stiffness. Some other interesting insights are obtained from the results, including slightly higher apparent stiffness when the whole height H was used for analysis, possibly due to the end restraint. This effect was alleviated by applying end lubrication, but not completely. The Poisson's ratio ν is supposed to be 0.5 for a specimen as a whole under undrained conditions. The middle part, however, showed slightly larger values due to barrelling. Although the strain ranges discussed here are beyond those typically associated with truly elastic behaviour (~0.001%), the image analysis is helpful in elucidating the non-uniform nature of the triaxial specimen at fairly small strains.

Table 1. Deformation parameters derived for small strains ($E_{u,sec}$ for ε_a=0.01% and ν for ε_a=0.05%).

Domain for calculation		Without lubrication		With lubrication	
		p': 70kPa	p': 250kPa	p': 70kPa	p': 250kPa
$E_{u,sec}$ (MPa)	H	52	154	38	120
	$H/3$	46	134	36	108
	Global	38	125	33	88
ν	H	0.418	0.570	0.595	0.588
	$H/3$	0.536	0.657	0.634	0.533
	Global	0.5			

3.3. Behaviour over wider strain ranges

The specimen deformation from the final monotonic axial loading to ε_a=15% is discussed below. The deformation during the isotropic compression and swelling was observed but not presented here; see Nishimura (2022) for more complete results.

The distributions of axial, radial and circumferential strains, ε_a, ε_r and ε_θ on the front and rear surfaces of the specimens with and without end lubrication are shown in Fig. 7. The comparison clearly reveals the effect of end lubrication leading to more uniform strain distributions. Without lubrication, all the strains were severely constrained at the vicinity of the specimen ends. Interestingly, only the circumferential strain ε_θ (calculated as negative stretching along the circumference) is influenced by the existence of filter paper strips installed between the specimen and the rubber membrane for drainage purpose. When average was taken, ε_r=-8.78% and ε_θ=-8.56% for the non-lubricated case, and ε_r=-11.4% and ε_θ=-8.74% for the lubricated case, at the end of loading. The radial strain derived from the global measurements was -8.59% and -8.86% for the two cases, respectively. The reason for the lubricated case to have significantly different ε_r is likely to be rigid-body translation of the specimen to one side, which cannot be corrected completely unless perfectly opposite (i.e. 180° apart) two surfaces are observed. Including the results from other stages, ε_θ seemed generally more representative of the horizontal strain when image analysis was adopted.

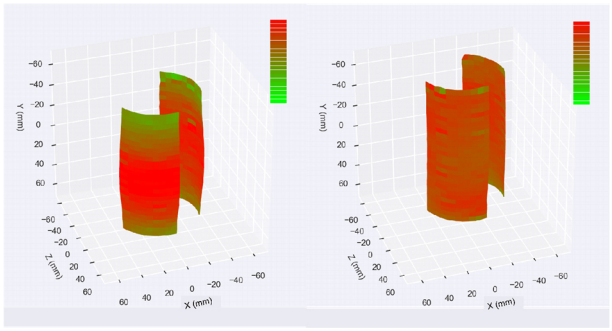

(a) Axial strain

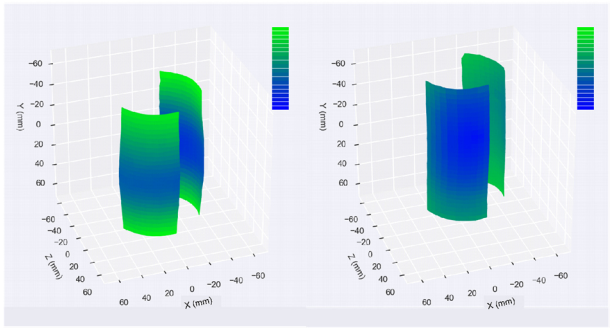

(b) Radial strain

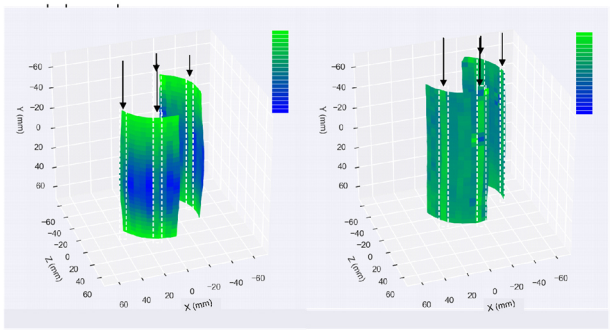

(c) Circumferential strain

Figure 7. Strains after monotonic loading to ε_a=15% (left: Non-lubricated case, right: Lubricated case).

The relationships between $E_{u,sec}$ and ε_a are shown for the middle third $H/3$ in Fig. 8. The precision of 0.001-0.002 mm means about 0.001% axial strain for a specimen height of 150 mm. The computed secant stiffness has a standard deviation (as a measure of scattering) smaller 10% of the mean only for strains greater than approximately 0.005%, and this is beyond the typical elastic threshold. Compared to the conventional local transducers such as LVDTs, which can usually resolve the strain to 10^{-4}%, the image analysis still has lower precision. Nevertheless, the $E_{u,sec} - \varepsilon_a$ curves obtained from the image analysis capture the stress-strain non-linearity well, and can be of practical use in many applications.

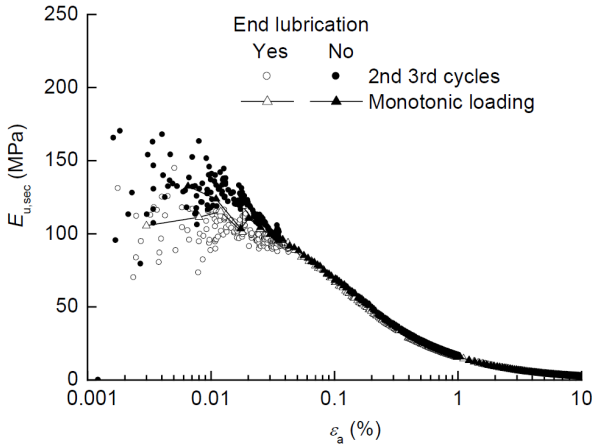

Figure 8. Variation of secant Young's modulus $E_{u,sec}$ against the axial strain ε_a, based on image analysis (over $H/3$).

4. Example of application: fine particle suffusion from sand in triaxial specimen

Another example involves suffusion of fine particles from a sandy specimen under isotropic stress in triaxial apparatus. This test was performed as part of research by Sarmah and Watabe (2023), and the images were taken and analysed by the author for them. The soil used was a pumice sand obtained from a liquefaction site in Sapporo (Watabe and Nishimura, 2020), containing about 45% non-plastic fines, 45% sand and 10% gravel. It was compacted at a degree of compaction of about 91%, and subjected to isotropic compression at 80 kPa. The specimen size was 100 mm in height and 50 mm in diameter. The pressure difference between the top and the bottom of the specimen was given, eventually reaching a hydraulic gradient of 200. The suffusion was thus allowed to occur for about 2 hours. See Sarmah and Watabe (2023) for more detail.

The conventional volume measurement based on the pore water drainage was difficult in this test, because the process involved a variable flux through the specimen

over long time. Installing local displacement sensors would not capture the volumetric behaviour completely, as the strain is not guaranteed to be uniform as the fine particles are carried from upstream and partially accumulate at the downstream end. The full-field measurement by the proposed stereophotogrammetric image analysis seemed the most effective way to investigate the behaviour, and eventually to evaluate the validity of the testing method.

Fig. 9 shows the distribution of strains caused by the suffusion process. The strains were relatively small, but it is clear that the downstream side of the seepage, or the specimen bottom, suffered local axial compression, suggesting net loss of fine particles close to the drainage end. Apparent radial strain is seen only on one side, but this is probably due to the movement of the specimen. The circumferential strain, which is calculated free from the rigid-body movement, and therefore believed to be more representative of the lateral strain, is close to zero across the specimen. The deformation is therefore localised and predominantly one-dimensional.

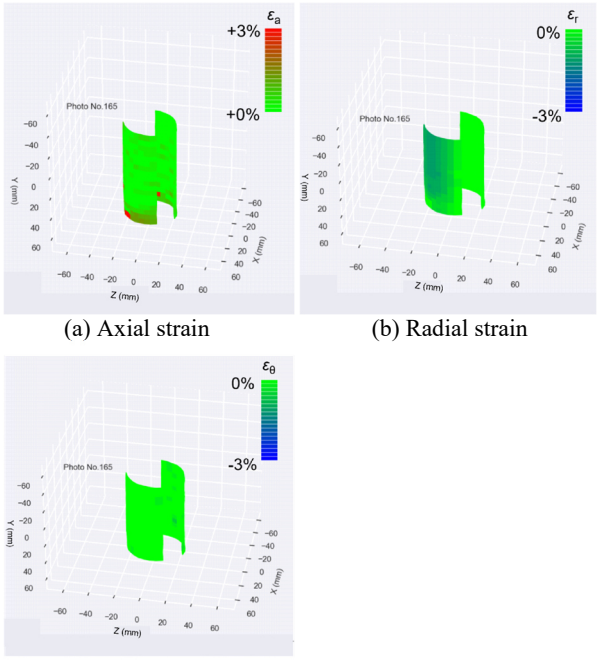

(a) Axial strain (b) Radial strain

(c) Circumferential strain

Figure 9. Strains in pumice sand due to fine particle suffusion caused by seepage flow under isotropic confinement.

5. Conclusions

This study proposed application of stereophotogrammetry for characterising and quantifying deformation of triaxial test specimens over a wide strain range spanning from 10^{-3}% order to 10^{1}% order, as an alternative to conventional global or local displacement measurements. High accuracy (1% of 5 mm displacement) and high precision (0.001-0.002 mm) were achieved in every three-dimensional direction by adopting sub-pixel Digital Image Correlation (DIC) for inter-image displacement tracking. The computation was facilitated by combing DIC with Particle Tracking Velocimetry (PTV), which assists DIC by significantly restricting the search range. The ray refraction due to the triaxial cell wall and cell water was corrected by ray tracing, following recent studies. More details are described by Nishimura (2022), including the validation exercise for accuracy and precision.

Two examples of application were shown; one with reconstituted saturated clay subjected to cyclic and monotonic undrained triaxial loadings, and another with pumice sand undergoing artificial suffusion under isotropic confining stress in triaxial apparatus. For the clay, lubricated and non-lubricated end cases were investigated. The Young's modulus and Poisson's ratio, determined for a strain level of 10^{-2}% to 10^{-3}% by image analysis, indicated how the measured parameters were affected by the end friction, and how much this effect was alleviated by end lubrication and/or considering only the middle portion of the specimen. The strain distributions visualised on the specimen surfaces clearly revealed the non-uniformity of deformation. The suffusion test was preliminary, but how the process affects the sample non-uniformly was also revealed, showing concentration of axial strain at the downstream of seepage flow.

The proposed method still has room for improvement of utility, including displacement tracking on the membrane surface where large deformation generates wrinkles masking the target points. A countermeasure for this was briefly discussed.

Acknowledgements

The author is grateful for JSPS KAKENHI Grant-in-Aid (19H02230), with which this study was conducted.

References

Bhandari, A. R., W. Powrie, and R. M. Harkness. 2011. "A Digital Image-Based Deformation Measurement System for Triaxial Tests." *Geotechnical Testing Journal* 35, no. 2: 209–226. https://doi.org/10.1520/GTJ103821

Kishi, M., and K. Tani. 2003. "Development of Measuring Method for Axial and Lateral Strain Distribution Using CCD Sensor in Triaxial Test." In *Deformation Characteristics of Geomaterials*, Lyon, Edited by Di Benedetto, H., T. Doanh, H. Geoffroy, and C. Sauzéat: 31–36. Lisse, The Netherlands: Swets & Zeitlinger B. V.

Nishimura, S., A. Iwaki, S. Takashino, and H. Tanaka. 2016. "Image-Based Measurement of One-Dimensional Compressibility in Cement-Treated Soils." *Géotechnique* 66, no. 10: 840–853. https://doi.org/10.1680/jgeot.15.P.218

Nishimura, S. 2022. "Characterisation of Soil Deformation over Wide Strain Ranges in Triaxial Test with High-Precision Stereophotogrammetry." *Géotechnique* Ahead of Print. https://doi.org/10.1680/jgeot.21.00067

Qiao, H., Y. Nakata, M. Hyodo, and N. Kikkawa. 2008. "Triaxial Compression Test for Unsaturated Sandy Soil Using Image Processing Technique." In *Deformation Characteristics of Geomaterials*, Atlanta, Edited by S. E. Burns, P. W. Mayne, and J. C. Santamarina: 529–534. Amsterdam, The Netherlands: IOS Press.

Sarmah, R., and Y. Watabe. 2023. "Suffusion in Compacted Satozuka Pumice Sand and Its Impact on Static Loading Undrained Shear Strength and Dilation Behaviour." Submitted to *Soils and Foundations*.

Viggiani, G., and S. A. Hall. 2008. "Full-Field Measurements, a New Tool for Laboratory Experimental Geomechanics." In *Deformation Characteristics of Geomaterials*, Atlanta,

Edited by S. E. Burns, P. W. Mayne, and J. C. Santamarina: 3–26. Amsterdam, The Netherlands: IOS Press.

Watabe, Y., and S. Nishimura. 2020. "Ground Movements and Damage in Satozuka District, Sapporo, Due to 2018 Hokkaido Eastern Iburi Earthquake." *Soils and Foundations* 60, no. 5: 1331–1356. https://doi.org/10.1016/j.sandf.2020.04.007

Zhang, X., L. Li, G. Chen, and R. Lytton. 2014. "A Photogrammetry-Based Method to Measure Total and Local Volume Changes of Unsaturated Soils during Triaxial Testing." *Acta Geotechnica* 10: 55–82. http://doi.org/10.1007/s11440-014-0346-8